Research Article | Vol. 31, No. 21 / 9 Oct 2023 / Optics Express 34917
Optics EXPRESS

Accurately predicting the tool influence function to achieve high-precision magnetorheological finishing using robots

RUNMU CHENG,[1,2] LONGXIANG LI,[1,2,3] DONGLIN XUE,[1,2,4] XINGCHANG LI,[1,2] YANG BAI,[1,2] XIAO LUO,[1] AND XUEJUN ZHANG[1,2]

[1] *Key Laboratory of Optical System Advanced Manufacturing Technology, Chinese Academy of Sciences, State Key Laboratory of Applied Optics, Changchun Institute of Optics, Fine Mechanics and Physics, Chinese Academy of Sciences, Changchun, Jilin 130033, China*
[2] *University of Chinese Academy of Sciences, Beijing 100049, China*
[3] *lilx@ciomp.ac.cn*
[4] *xuedl@ciomp.ac.cn*

Abstract: Industrial robots with six degrees-of-freedom have significant potential for use in optical manufacturing owing to their flexibility, low cost, and high space utilisation. However, the low trajectory accuracy of robots affects the manufacturing accuracy of optical components when combined with magnetorheological finishing (MRF). Moreover, general robot trajectory-error compensation methods cannot compensate for the running errors of large robots with high precision. To address this problem, a three-dimensional (3D) tool influence function (TIF) model based on inverse distance interpolation is developed in this study to accurately predict the TIF of different polishing gaps. A high-precision robot-MRF polishing strategy based on variable TIFs and surface shape accuracy of polished optics is proposed to achieve high-precision manufacturing without compensating for trajectory errors. Subsequently, the accuracy of a ϕ420 mm fused silica mirror is experimentally verified to be from 0.11 λ RMS to 0.013 λ RMS. This validates that the robot-MRF can achieve high-precision polishing without compensating for trajectory errors. Furthermore, the proposed model will promote the applications of industrial robots in optical manufacturing and will serve as a reference in the field of intelligent optical manufacturing.

1. Introduction

With the popularity of segmented optics in next-generation telescopic systems, such as the Giant Magellan Telescope [1,2], European Extremely Large Telescope [3,4], and Thirty Meter Telescope [5], higher requirements have been proposed for the quantity, surface complexity, and quality of optical components in optical systems. However, it is challenging to obtain optical elements with high accuracy, high efficiency, and low cost using traditional optical manufacturing technologies. In recent years, an increasing number of industrial robots have been used to replace traditional CNC-machine to address these problems. A robot with a higher degree of freedom is more suitable for a complex surface; a lower use area is conducive to the placement of more robots, which is beneficial for improving efficiency, and a lower equipment cost is also beneficial for reducing expenses. Derst et al. [6] utilised a robot polisher to manufacture a 1560 mm on-axis asphere, and the surface quality at the end of the process was 0.045 µm RMS. David Walker et al. [7] also utilised a robot to polish a large-aperture optical element assembled from 5-off 1 m A/C hexagonal float-glass sheets epoxied together. Other optical manufacturing technologies have been used in combination with robots, such as robot-computer controlled optical surfacing [8,9], robot-wheeled polishing [10], and robot-bonnet polishing [11]. These studies indicated the

#498458 https://doi.org/10.1364/OE.498458
Journal © 2023 Received 20 Jun 2023; revised 29 Aug 2023; accepted 1 Sep 2023; published 3 Oct 2023

Optics EXPRESS

diversity of combinations of robotic and optical manufacturing technologies, revealing a great potential of robotic applications in optical manufacturing.

Magnetorheological finishing (MRF) [12–14] is a typical optical manufacturing technology in the field of high-precision optical manufacturing that has the advantages of a stable tool influence function (TIF) and high finishing certainty. However, the lower trajectory accuracy of the robot causes TIF changes, which cannot satisfy the high-precision manufacturing requirements of MRFs. The conventional approach for solving this problem is to improve the trajectory accuracy of the robot-MRF to maintain the stabilisation of the TIF. Zhang et al. [15] used a real-time system to control the stabilisation of the robot-MRF polishing gap and implemented a 7.59 nm RMS polishing accuracy on a 100 mm × 100 mm fused silicon mirror. Cheng et al. [16] utilised a step-by-step and multistage iterations trajectory error compensation method based on spatial similarity to improve the trajectory accuracy of Z-axis from PV > 0.2 mm to PV < 0.1 mm and the finishing accuracy of a ϕ340 mm spherical mirror from 0.184 λ RMS to 0.013 λ RMS using the compensated robot-MRF. However, these methods rely on additional equipment to measure trajectory errors, consequently driving up the cost of the robot-MRF setup. Moreover, the need for complex robot position/orientation compensation knowledge places higher skill demands on operators and thus constrains the broader application of robots in the field of high-precision manufacturing.

As an alternative to conventional methods, we propose a novel approach that mitigates the impact of robot trajectory errors on manufacturing accuracy. This strategy predicts trajectory errors based on the residual surface shape errors of the optics, rather than relying on trajectory-error measurement equipment. It employs variable TIFs to achieve high-precision polishing, negating the need for trajectory error compensation. This method offers several advantages, notably the elimination of the need for costly measurement equipment and complex trajectory error compensation. By utilising the inherent technical characteristics of optical manufacturing technology, we can suppress the running error of the robot and attain our high-precision polishing objective.

Despite promising advances, such as those made by Zhong et al. [17] predicted the trajectory errors of a robot-BP by polishing a 400 mm × 400 mm aperture aspheric element thrice. However, because the relationship between the TIF and trajectory errors is neglected, the trajectory errors cannot be predicted accurately by the surface figures of the polished optics, and the final polishing result still contains the periodic surface residual caused by the trajectory errors even after three compensation cycles. Moreover, their strategy still relied on trajectory error compensation to suppress systematic robot trajectory errors, neglecting the variable TIFs of optical manufacturing technology and the potential of this technology to reduce the impact of the robot's operating error on polishing accuracy.

Accurately predicting the variety of TIF based on the surface figures of polished optics is the key to ensuring high-precision manufacturing of the robot-MRF without a measurement facility. In this study, a 3D MRF TIF model was established based on the relationship between material removal rate (MRR) of the MRF and the polishing gap. An accurate prediction method for polishing gaps variation based on the surface figures of polished optics was proposed to determine the TIF changes during the polishing process of the robot-MRF. Finally, high-precision polishing experiments were performed using the robot-MRF without compensating for the trajectory errors. This study demonstrates that the use of technical characteristics of optical manufacturing technology can compensate for the robots' inherent operational accuracy limitations, which has the potential to significantly aid in the low-cost adoption and application of robots in the field of optical manufacturing.

Optics EXPRESS

2. 3D model of MRF tool influence function with different polishing gaps

2.1. Relationship between MRR and polishing gap

The trajectory errors of robots lead to variations in the polishing gap, and the relationship between the TIF normal pressure and polishing gap is nonlinear [18]. Therefore, the change of polishing gaps will lead to the nonlinear change of the TIF MRR. The MRF TIF model is expressed as follows Eq. (1), and the corresponding schematic diagram is shown in Fig. 1.

$$dz(x, y) = kP(x, y)v(x, y)dt \tag{1}$$

where $z\ (x, y)$ is the material-removal depth at the polished point (x, y), k is Preston's coefficient, $P\ (x, y)$ denotes the pressure distribution, $v\ (x, y)$ is the relative velocity between the polishing wheel and optics. $P\ (x, y)$ can be described as Eq. (2):

$$P(x, y) = P_d(x, y) + P_m(x, y). \tag{2}$$

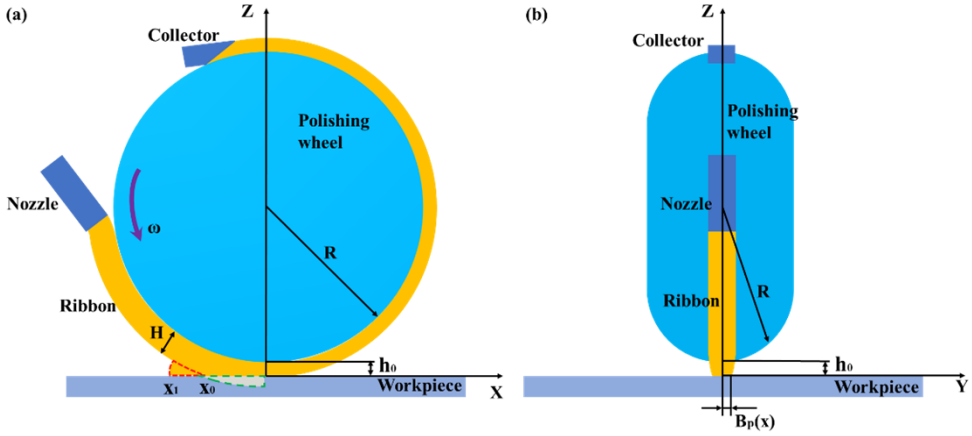

Fig. 1. The schematic diagram of MRF polishing. (a) Seen from the Y-axis. (b) Seen from the X-axis.

$P_d\ (x, y)$ is hydrodynamic pressure, and $P_m\ (x, y)$ is magnetization pressure. Since $P_m\ (x, y)$ is several orders of magnitude smaller than $P_d\ (x, y)$, it can be considered that the hydrodynamic pressure plays a major role in the MRF polishing. $P_d\ (x, y)$ can be expressed as follow [19]:

$$P_d(x, y) = \frac{8\eta R^2 xv(4y^2 + B_p(x))}{(B_p(x)(2Rh_0 + x^2))^2} \quad |y| < B_p(x). \tag{3}$$

where $v = 2\pi nR$, n denotes the speed of the polishing wheel, R is the radius of the polishing wheel, η represents the working viscosity of the magnetorheological fluid, h_0 is the distance between the lowest point of the polishing wheel and the workpiece, namely, the polishing gap, and $B_p(x)$ is the width of the polished spot corresponding to different positions in the spot. Therefore, the MRF TIF model can be expressed as:

$$dz(x, y) = \frac{32\pi^2 kn^2 \eta R^4 x(4y^2 + B_p(x))}{(B_p(x)(2Rh_0 + x^2))^2} dt. \tag{4}$$

Optics EXPRESS

TIF MRR can be expressed as follows:

$$\begin{aligned} MRR &= \int_{x_1}^{-x_1}\int_{x_1}^{0} dz(x,y)dxdy \\ &= \int_{x_1}^{-x_1}\int_{x_1}^{0} \frac{32\pi^2 kn^2\eta R^4 x(4y^2+B_p(x))}{(B_p(x)(2Rh_0+x^2))^2}dtdxdy \\ &= \sum_{y=x_1}^{-x_1}\sum_{x=x_1}^{0} \frac{32\pi^2 kn^2\eta R^4 x(4y^2+B_p(x))}{(B_p(x)(2Rh_0+x^2))^2}dt\Delta x\Delta y \end{aligned} \tag{5}$$

$$\begin{cases} x_0 = \sqrt{(R+H)^2-(R+h)^2} \\ \int_{x_1}^{x_0} R+h-\sqrt{(R+H)^2-x^2}dx = \int_{x_0}^{0} R+h-\sqrt{(R+H)^2-x^2}dx \\ h = R-\sqrt{R^2-x^2-y^2}+h_0 \approx h_0+\frac{x^2+y^2}{2R} \end{cases}$$

where H is the thickness of the Magnetorheological fluid ribbon on the polishing wheel.

Equation (5) can simplify the relationship between MRR and h_0 as follows:

$$MRR(h_0) \propto \frac{1}{bh_0{}^2+ch_0+d} \tag{6}$$

Where b, c and d represent proportional coefficients respectively, which can be obtained by curve fitting based on the measured TIF test results.

TIF experiments were performed with different polishing gaps on a fused silica plane mirror. The experimental parameters are listed in Table 1. A comparison between the simulation and experimental results is shown in Fig. 2. Curve fitting was performed based on the experimental results, and the fitting curve formula was shown in Eq. (7). The R-squared value (coefficient of determination) was 0.9926 and the root mean squared error (RMSE) was 0.005167 using the fitting equation. The theoretical and experimental fitting curves almost overlapped, as shown in Fig. 2, indicating that the established model can accurately predict the MRR as the polishing gap changes.

$$MRR(h_0) \propto \frac{1}{4.962h_0{}^2-11.64h_0+10.5} \tag{7}$$

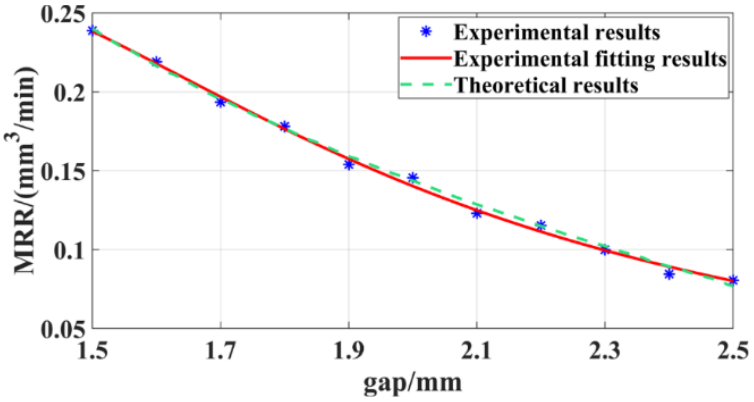

Fig. 2. Comparison of simulation and experiment results for the volume removal rate of TIFs.

Optics EXPRESS

Table 1. TIF experimental parameters

Parameter	Wheel diameter/(mm)	Rotate speed/(r/min)	Ribbon thickness/(mm)	Viscosity/(Pa s)
Value	360	60	4.2	0.3

2.2. TIF prediction with different polishing gaps

Although Eq. (7) accurately reveals the relationship between the TIF MRR and the polishing gap, there is still a finite deviation between the shape of the theoretical TIF and the actual TIF [19], which affects the accuracy of the dwell-time solution. To accurately obtain the TIFs with different polishing gaps, the inverse distance interpolation (IDT) method [20] was used to accurately predict the TIFs based on the relationship of the MRR and the polishing gap. The prediction model and schematic are shown in Eq. (8) and Fig. 3, as follows:

$$\begin{cases} d_{mi} = \sqrt{(x_j - x_{mi})^2 + (y_j - y_{mi})^2 + (z_j - z_{mi})^2} & \\ q_{mi} = \dfrac{\left(1/d_{mi}\right)^r}{\sum_{i=1}^{8}\left(1/d_{mi}\right)^r} & i = 1,2,3,4 \\ & m = 1,2 \\ dz_j'(x_j, y_j) = \sum_{i=1}^{8} dz_{mi}(x_{mi}, y_{mi}) \cdot q_{mi} & \end{cases} \tag{8}$$

where $G_1(x_{1i}, y_{1i}, z_{1i})$ and $G_2(x_{2i}, y_{2i}, z_{2i})$ are the coordinates of the polishing gap layers for which the TIFs are known, $G'(x_j, y_j, z_j)$ is the coordinate of the polishing gap layer where the TIF is to be solved, $g_1(x_{1i}, y_{1i}, dz_{1i})$ and $g_2(x_{2i}, y_{2i}, dz_{2i})$ are the coordinates of each point of the known TIFs, $g'(x_j, y_j, dz_j')$ is the coordinates of each point of the solved TIFs, d_1 and d_2 represent the respective points on the polishing gap layer, where the known TIFs are located, and the polishing gap layer, where the solved TIFs are located, respectively, q denotes the weight of $g_1(x_{1i}, y_{1i}, dz_{1i})$ and $g_2(x_{2i}, y_{2i}, dz_{2i})$, r is the weighted power, and $r = 2$ is based on the relationship between the MRR and polishing gaps.

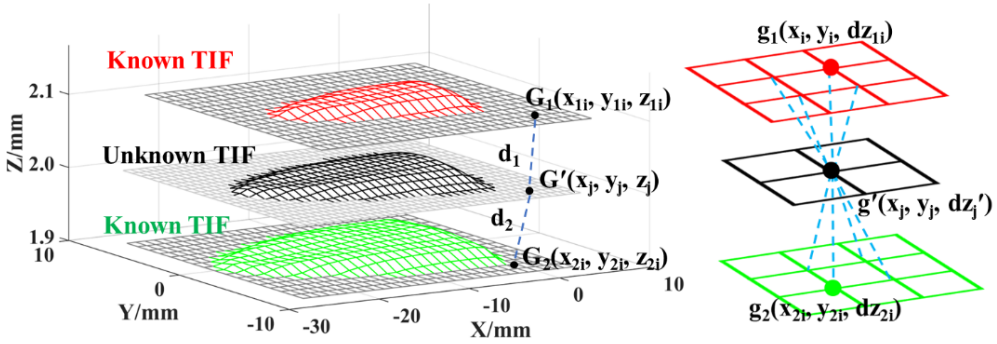

Fig. 3. Schematic of the inverse-distance interpolation method for predicting TIF.

To verify the prediction accuracy of the IDT method for the TIFs of different polishing gaps, the TIF of $h = 1.8$ mm was predicted by the TIFs of $h_0 = 1.7$ mm and $h_0 = 1.9$ mm, and the TIF of $h = 2.1$ mm was predicted by the TIFs of $h_0 = 2.0$ mm and $h_0 = 2.2$ mm. As presented in Table 2, the prediction errors of the IDT are less than 3%; therefore, the prediction accuracy is better than that of the currently commonly used linear prediction (LP) method [21], and the prediction errors of the MRR are less than 1%. Therefore, the IDT can be used to accurately predict TIFs with different polishing gaps.

Optics EXPRESS

Table 2. TIFs prediction accuracy comparison

Polishing gap	Method	MRR/(mm^3/min)	PRR/(μm/min)	Length/(mm)	Width/(mm)
$h = 1.8$mm	Experiment	0.1781	1.7393	23.73	9.49
	IDT	0.1771(0.56%)	1.7168(1.29%)	23.18(2.32%)	9.26(2.42%)
	LP	0.1832(2.86%)	1.7843(2.59%)	24.59(3.62%)	9.78(3.06%)
$h = 2.1$mm	Experiment	0.1273	1.6556	21.70	7.73
	IDT	0.1267(0.47%)	1.6119(2.64%)	22.33(2.90%)	7.94(2.72%)
	LP	0.1227(3.61%)	1.7020(2.80%)	22.51(3.73%)	8.01(3.62%)

3. Robot-MRF high-precision polishing based on variable TIFs

3.1. Analysis of material removed based on variable TIFs

The core principle for determining the shape error of the optics of an MRF is shown in Eq. (9).

$$E(x, y) = R(x, y) \otimes \otimes T(x, y) \tag{9}$$

where *E (x, y)* is the amount of material removal at position (x, y), *R (x, y)* is the MRR at position (x, y), *T (x, y)* is the dwell time at position (x, y), and ⊗⊗ is the two-dimensional convolution.

The convolution expression can be transformed into a matrix product, as shown in Eq. (10).

$$[E] = [R] \cdot [T] = \begin{bmatrix} r_{11} & r_{12} & \cdots & r_{1n} \\ r_{21} & r_{22} & \cdots & r_{2n} \\ \vdots & \vdots & \ddots & \vdots \\ r_{m1} & r_{m2} & \cdots & r_{mn} \end{bmatrix} \cdot \begin{bmatrix} t_1 \\ t_2 \\ \vdots \\ t_n \end{bmatrix} = \begin{bmatrix} e_1 \\ e_2 \\ \vdots \\ e_m \end{bmatrix} \tag{10}$$

where $[E] = [e_i]^T \quad i = 1, 2, \cdots, m$, $[T] = [t_j]^T \quad j = 1, 2, \cdots, n$, $[R] = [r_{ij}]^T$ and $[e_i]$ are the amounts of material removed at each point on the surface of the element, $[r_{ij}]$ is the MRR at each point on the surface of the element, $[t_j]$ is the dwell time of each trajectory point, i is the number of points removed, and j is the number of trajectory points.

Trajectory errors during the polishing process cause continuous changes in the TIF. Therefore, the actual amount of material removed can be expressed using Eq. (11).

$$[E_r] = [R \oplus \Delta R] \cdot [T] = \begin{bmatrix} r_{11} \oplus \Delta r_{11} & r_{12} \oplus \Delta r_{12} & \cdots & r_{1n} \oplus \Delta r_{1n} \\ r_{21} \oplus \Delta r_{21} & r_{22} \oplus \Delta r_{22} & \cdots & r_{2n} \oplus \Delta r_{2n} \\ \vdots & \vdots & \ddots & \vdots \\ r_{m1} \oplus \Delta r_{m1} & r_{m2} \oplus \Delta r_{m2} & \cdots & r_{mn} \oplus \Delta r_{mn} \end{bmatrix} \cdot \begin{bmatrix} t_1 \\ t_2 \\ \vdots \\ t_n \end{bmatrix} = \begin{bmatrix} e_1 \oplus \Delta e_1 \\ e_2 \oplus \Delta e_2 \\ \vdots \\ e_m \oplus \Delta e_m \end{bmatrix}. \tag{11}$$

where $\Delta R = [\Delta e_{ij}]^T$ is the change of TIF, ⊕is the generalised plus sign, which represents the addition of the length, width, peak removal rate, and volume removal rate of the TIF.

Combining Eq. (10) and (11), the change in material removal caused by the variable TIFs is given by Eq. (12).

$$[\Delta E_r] = [\Delta R] \cdot [T] \tag{12}$$

where $[\Delta E_r] = [E_r] - [E]$ and $[\Delta R] = [R \oplus \Delta R] - [R]$.

Optics EXPRESS

Evidently, *[ΔR]* can be solved by multiplying both sides of Eq. (12) using *1/[T]*. However, *[T]* is a non-inverse matrix, and there is no unique solution of *[ΔR]* because *i* is usually not equal to *j*. Additionally, the systematic trajectory errors of robot-MRF exhibit obvious periodic characteristics [16], and the polished surface errors contain periodic information of systematic trajectory error mapping. Therefore, the key to determining the TIF change rule is to extract the periodic information caused by the systematic trajectory errors and build a mapping relationship between them.

3.2. Accurate solution of TIF change based on polished surface errors

The accurate extraction of information about the change in TIFs from the surface residuals depends on four conditions. First, the change in TIFs caused by trajectory errors has high repeatability; that is, when the trajectory parameters remain unchanged, the spatial position remains unchanged, the polishing time is short, and the change in trajectory errors is ignored owing to mechanical deformation and gear friction changes. Therefore, the systematic trajectory errors remain unchanged or have negligible minor changes. Second, systematic trajectory errors are the most important factor, and random trajectory errors do not inhibit high-precision polishing. Then, the influence of the stability of the circulating system and the change in the properties of the magnetorheological fluid on the TIFs and high-precision polishing is negligible. Finally, the change information of TIFs caused by systematic trajectory errors needs to be highlighted in the surface residuals without interference from middle-high frequency errors.

Reference [16] shows that systematic trajectory errors are highly repeatable when the trajectory parameters and spatial positions remain unchanged. The Z-axis systematic trajectory error is the main factor leading to a change in the polishing gap. After compensation, the random error can meet the requirements of high-precision polishing. The influence of the circulatory system and properties of the magnetorheological fluid on high-precision polishing is negligible. Therefore, highlighting the change in TIFs caused by systematic trajectory errors on the surface residual and extracting the correct change in polishing clearance are key to the TIFs variation calculation.

Aiming at the residual surface shape errors of the robot-MRF systematic trajectory errors, a high-precision robot-MRF polishing method based on variable TIFs and surface figures of polished optics was proposed. The method was divided into five steps: (a) TIF parameter selection, (b) design of the polishing strategy, (c) systematic errors separation and extraction, (d) solution for the change of TIFs, and (e) Polishing with variable TIFs. The flow chart is shown in Fig. 4 and specific implementation steps are as follows.

(a) TIF parameter selection

Compared with the Computer Controlled Optical Surface and other circularly symmetric TIFs, the TIFs of MRF only had symmetry along the long axis, as shown in Fig. 5. The most evident systematic trajectory errors were similar to a sinusoidal distribution along the X-axis [16]. The differences in the angles of the TIFs, which were relative to the trajectory error characteristics, led to different forms of residual periodic errors in the surface error after polishing. To make the residual surface shape errors more similar to the trajectory errors and more suitable for solving the variation in MRF TIFs, the long-axis direction of the MRF TIFs should be perpendicular to the direction of the periodic change in the systematic trajectory errors.

Simulation verification was carried out to validate the above observations as follows. The angle of TIF was set to 0° when the direction of TIF long axis was parallel to X-axis, and 90° when it is perpendicular to the X-axis. Both angles are the most commonly used MRF's TIF angles. An ideal sinusoidal variation with 80 mm space period and ±0.1 mm amplitude was used to simulate the variation characteristics of the polishing gap caused by the trajectory errors of robot-MRF, and the TIFs were predicted by IDT according to different polishing gaps. Schematic diagrams of the variations in the 0° and 90° TIFs along the polishing track are shown in Fig. 6. Under the condition of equal thickness removal of 0.5 λ, the simulation results of the residual periodic

Optics EXPRESS

surface figures after polishing with the variable TIFs corresponding to 0° and 90° are shown in Fig. 7. The X-Z curves of the simulation results correspond to 0° and 90°, and the variations in the polishing gap when $Y = 0$ were extracted and normalised, as shown in Fig. 8. Evidently, when the TIFs angle is 90°, the variable trend of the periodic surface error is more similar to that of the polishing gap, and there is a linear transformation relationship between them. Therefore, setting the TIF angle to 90° (the major axis of the TIF is perpendicular to the direction along the variation in the periodic trajectory error) is more conducive for solving the change in the TIFs.

(b) Design of first polishing strategy

This is an important index for the selection of a polishing strategy, in which the periodic variation information of the polishing gap can be highlighted on the polished mirror surface without being masked by random noise in the surface error. Information highlighting methods for periodic polishing gap changes can be divided into two types: surface error conformal polishing, in which the material is removed with equal thickness [22], and surface error convergence polishing, in which the initial surface error is polished to make it converge. The simulation results of the periodic surface errors corresponding to the two methods are shown in Fig. 9 with TIFs at an angle of 90°. The change trend of the polishing gap shown in Fig. 7(a) and the corresponding simulation results of periodic surface errors shown in Fig. 9(c) and Fig. 9(f) were extracted and compared when $Y = 0$, as shown in Fig. 10. Notably, the sinusoidal change trend of the simulation results of the surface error conformal polishing method was consistent with that of the polishing gap, which is more suitable for solving the TIFs change. Therefore, to highlight the periodic surface errors caused by trajectory error, the first polishing strategy is to remove the material with uniform thickness Δh on the surface of the optics to be polished.

(c) Error separation and extraction

The residual surface error information $E_{res}(x, y)$ of the first polished surface obtained by the conformal polishing method includes the initial surface error $E_{ini}(x, y)$ before polishing, periodic surface error $E_{sys}(x, y)$ caused by systematic changes in the polishing gap, and surface errors introduced by the dwell time algorithm $E_{dt}(x, y)$. Therefore, periodic surface error $E_{sys}(x, y)$ can be represented by Eq. (13), as follows:

$$E_{sys}(x, y) = E_{res}(x, y) - E_{ini}(x, y) - E_{dt}(x, y) \tag{13}$$

However, $E_{sys}(x, y)$ still contains random information caused by the flow disturbance of the magnetorheological fluid supply system, random trajectory errors of the robot, and random circular runout of the polishing wheel. Therefore, Autoregressive Integrated Moving Average Model (ARIMA) [23,24] was used to extract the systematic errors accurately. A typical *ARIMA(p, d, q)* model is expressed by Eq. (14), as follows.

$$\begin{cases} \phi(B)(1-B)^d Z_t(x, y) = \theta(B)\varepsilon_t \\ \phi(B) = 1 - \phi_1 B - \cdots - \phi_p B^p \\ \theta(B) = 1 - \theta_1 B - \cdots - \theta_q B^q \end{cases} . \tag{14}$$

where $\phi(B)$ is a p-order autoregressive polynomial, $\theta(B)$ is q-order moving average polynomial, B represents the Lag operator, $B^m Z_t = Z_{t-m}$. ϕ_i (i = 1,2. . . p) is auto-regressive parameter, θ_i (i = 1,2. . . q) is moving average parameter, ε_t is white noise series with zero mean, and $Z_t(x, y)$ is the systematic information in $E_{sys}(x, y)$.

(d) Solution of TIF change

As shown in Fig. 10, there is a linear transformation relationship between the polishing gap distribution changes and periodic surface error map. The linear triangulation interpolation method [25] was used to obtain the sparse periodic error $p(x, y)$ of the corresponding theoretical trajectory points based on the periodic surface error $Z_t(x, y)$. Therefore, the relationship between

Optics EXPRESS

the systematic polishing gap variation $P(x, y)$ and sparse periodic error $p(x, y)$ can be represented by Eq. (15), as follows:

$$P(x_i, y_j) = k_j \cdot p(x_i, y_j) \quad (i = 1, 2, 3 \ldots n, j = 1, 2, 3 \ldots m) \tag{15}$$

where k_j is the linear scaling factor, j the grating trajectory path line, and i the trajectory point of each path line.

Equation (15) was deployed to calculate the variation in the polishing gap at each trajectory point during the process. The IDT method was employed to compute the TIFs associated with different polishing gaps at trajectory points. To confirm the accuracy of TIF alterations, a series of simulation calculations were undertaken. New surface errors were computed with variable TIFs and the dwell time was established at each trajectory point when the material was removed at an equal thickness denoted by Δh. The periodic errors in the simulated surface errors were compared with those in the first polished surface figures. If there were discrepancies containing periodic error components, the coefficient k_j was adjusted and the simulation analysis was repeated. This iterative process continued until no systematic error between the two was observed, with the minimum RMS serving as an additional constraint to solve the TIFs accurately.

(e) Polishing with variable TIFs.

In the subsequent polishing stage, the precisely resolved variable TIFs were used as inputs for determining the polishing parameters. A dwell-time matrix and a polishing control file were generated under variable TIFs to further validate the accuracy of the TIF prediction on the surface after the first polishing, and the robot-MRF system applied these variable TIFs for high-precision polishing.

In conclusion, the method eliminates the need for expensive robot operation error measurement equipment and complex knowledge of robot operation error compensation. Instead, it employs the principles of MRF to control the impact of robot-MRF operation error on polishing accuracy. This leads to the realisation of high stability and high precision polishing.

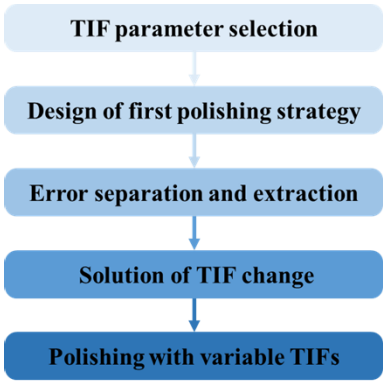

Fig. 4. Flow chart of robot-MRF high-precision polishing with variable TIFs.

Optics EXPRESS

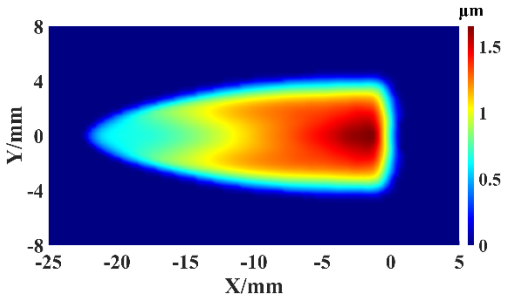

Fig. 5. MRF TIF.

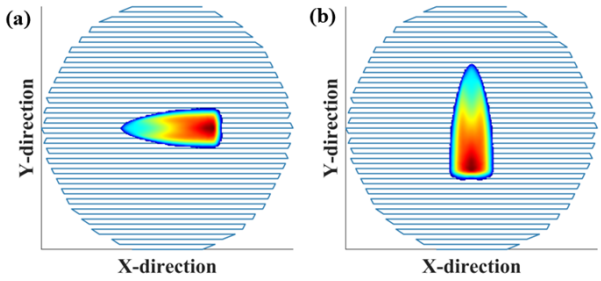

Fig. 6. Zero- and ninety-degree TIFs along the polishing track. (a) Zero-degree and (b) ninety-degree TIFs.

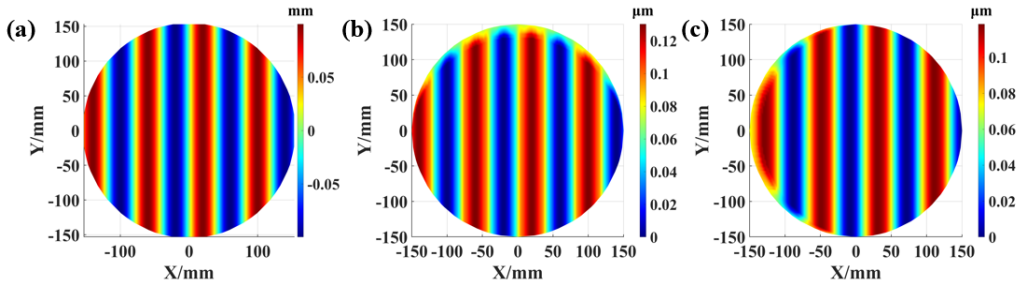

Fig. 7. Ideal sinusoidal polishing gap change and simulation results of zero-degree and ninety-degree TIFs. (a) Ideal sinusoidal polishing gap change; (b) simulation results of zero-degree TIF; and (c) simulation results of ninety-degree TIF.

Optics EXPRESS

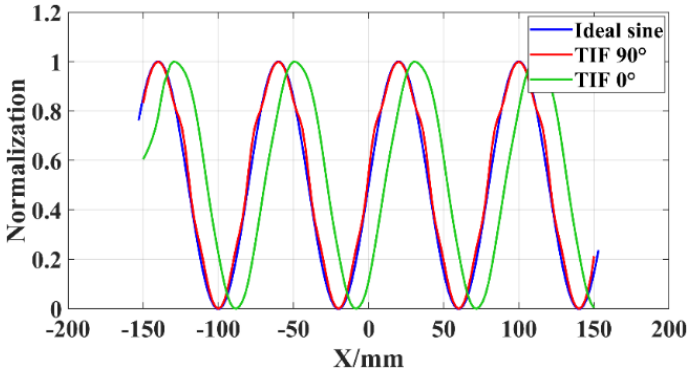

Fig. 8. Normalized X-Z curves of polishing gap variations and simulation results of zero-degree and ninety-degree TIFs with Y = 0.

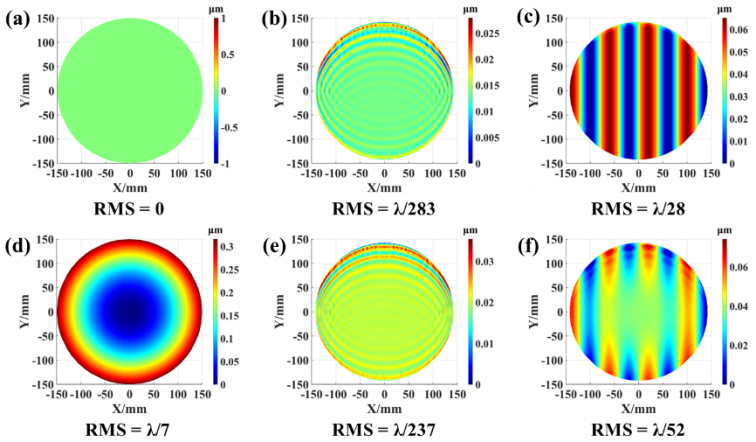

Fig. 9. Simulation results of the equal thickness and convergence polishing. (a) Initial surface accuracy RMS = 0; (b) residual surface errors of equal thickness removal 0.5 λ with constant TIF; (c) residual surface errors of equal thickness removal 0.5 λ with changed TIFs; (d) The initial surface accuracy with power PV = 0.5 λ; (e) residual surface errors of convergence polishing with constant TIF; and (f) residual surface errors of convergence polishing with changed TIFs.

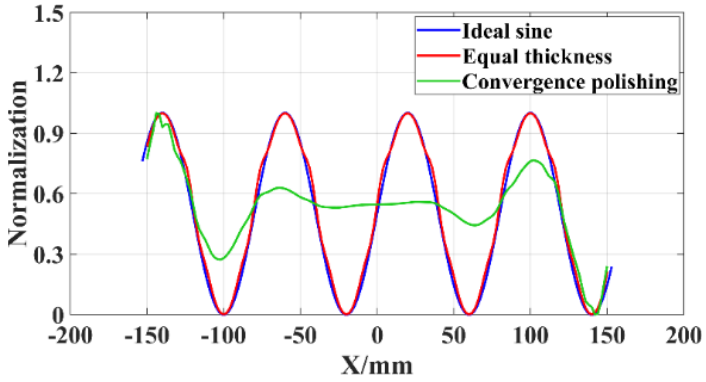

Fig. 10. Normalized X-Z curves of polishing gap variations and simulation results of equal thickness and convergence polishing with Y = 0.

Optics EXPRESS

4. Results and discussion

4.1. Build of robot-MRF

A robot-MRF was built, as shown in Fig. 11, to realise the combined application of an MRF and a robot. The robot was an ABB IRB 6700-200, with an operating range of 2.6 m, a loading capacity of 200 kg, an absolute positioning accuracy of approximately ±0.25 mm, and a repeat positioning accuracy of ±0.05 mm. The MRF module weighed 107 kg, and the diameter of the polishing wheel was 360 mm. Through precise TCP calibration, the position and orientation of the robot end and polishing wheel working point were accurately determined. The rotation velocity of the polishing wheel was set to 60 rpm/min, while the viscosity, maximum movement speed, and flow rates of the MR fluids were constant at 15 Pa·s, 100 mm/s, and 1800 mL/min, respectively.

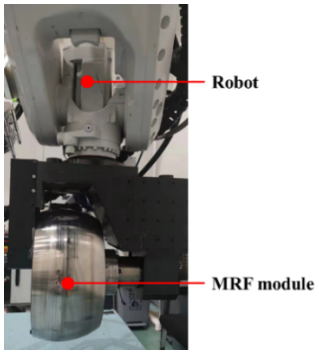

Fig. 11. Structure of the robot-MRF.

4.2. High-precision polishing experiment verification of plane mirror

A polishing experiment was conducted on plane mirrors to verify whether the robot-MRF with the changed TIFs had high-precision polishing capability. The polishing parameters are listed in Table 3, the initial surface accuracy of the plane mirror is shown in Fig. 12, and the experimental site is shown in Fig. 13.

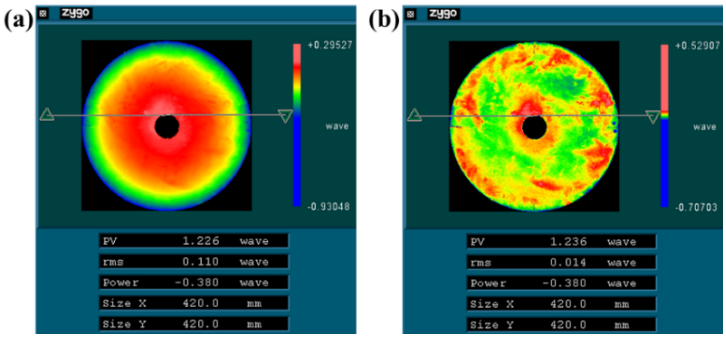

Fig. 12. Initial surface accuracy of plane mirror. (a) Full aperture measurement results, RMS = 0.11 λ. (b) Full aperture measurement results with the primary aberrations (Power, Coma, Astigmatism, and Spherical aberration) are eliminated, RMS = 0.014 λ.

The formulation of the first polishing strategy and the polishing results. Reference [16] indicates that systematic trajectory errors evolve periodically along the X-axis direction. Consequently, the

Optics EXPRESS

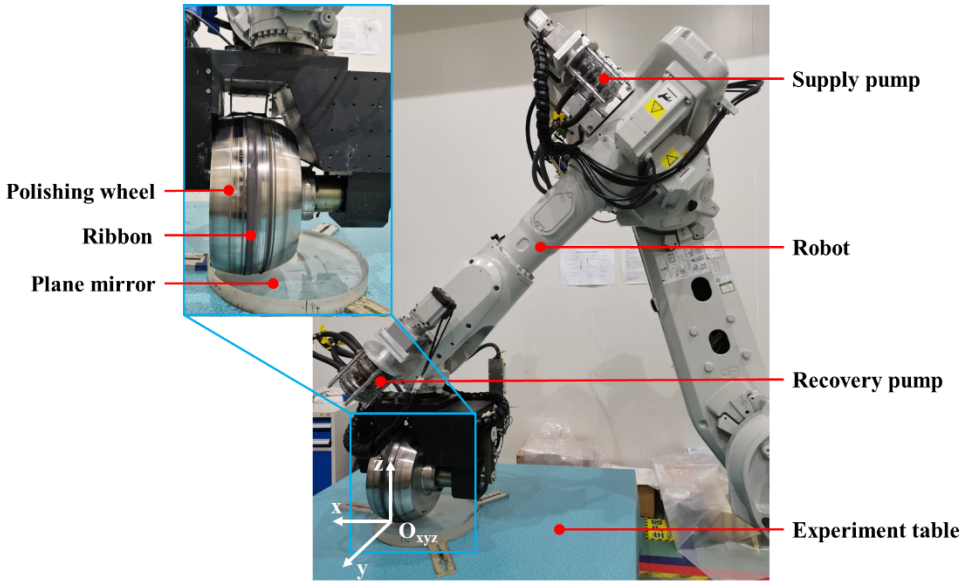

Fig. 13. Polishing experimental setup showing the plane mirror.

Table 3. Plane mirror polishing parameters

Parameter	Plane mirror
Material	fused silica
Outside diameter	Φ420 mm
Inside diameter	ϕ60 mm
Initial surface error (RMS, λ = 632.8 nm)	0.11 λ
Grating track diameter	500 mm
Grating track step ΔX	4 mm
Grating track spacing ΔY	1 mm

long-axis direction of the TIF was set perpendicular to the X-axis of the tool coordinate system, as depicted in Fig. 6(b). To accurately predict the TIF and prevent systematic error from being overshadowed by random error, the initial polishing strategy was to remove material uniformly to a depth of 0.5 λ. Using unchanged input TIFs, dwell times were calculated and the polishing control program were generated. The results of the first polishing phase for the plane mirror are presented in Fig. 14. Comparing the surface shape errors before and after polishing revealed that the mirror surface carries periodic error information post-polishing, attributable to the periodic variation in the polishing gap, as illustrated in Fig. 15.

Pursuing the methodology described in Section 3, the variations of TIFs caused by trajectory errors were accurately predicted, specifically Z-axis trajectory errors related to the polishing plane of the robot-MRF, based on Eq. (13) and (15). Figure 16 showcases these TIF variations by mapping the distribution of changes in the polishing gap. The corresponding simulation results, presented in Fig. 17, with variable TIFs, show no periodic errors, thus suggesting that systematic TIF changes were accurately predicted. As Fig. 18 demonstrates, the polishing gap variation predicted by the proposed method aligns well with the experimental results, validating our ability to accurately forecast the changes in TIFs.

Optics EXPRESS

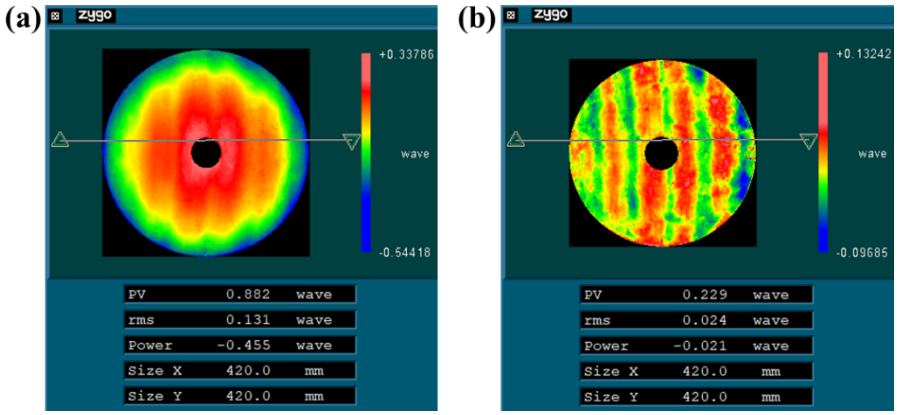

Fig. 14. First polishing results of plane mirror using the robot-MRF. (a) Surface figures of equal thickness removal: RMS = 0.134 λ and (b) periodic surface residuals caused by the changed polishing gap.

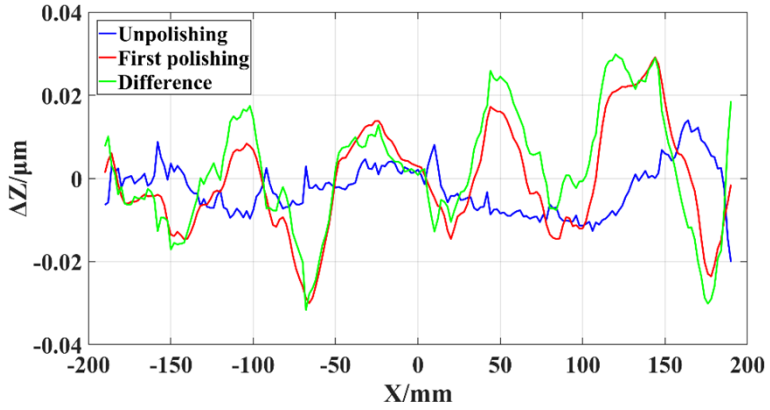

Fig. 15. Contrast curve of surface shape errors without the primary aberrations (Power, Coma, Astigmatism, and Spherical aberration) before polishing and periodic surface residuals after first polishing along X-axis.

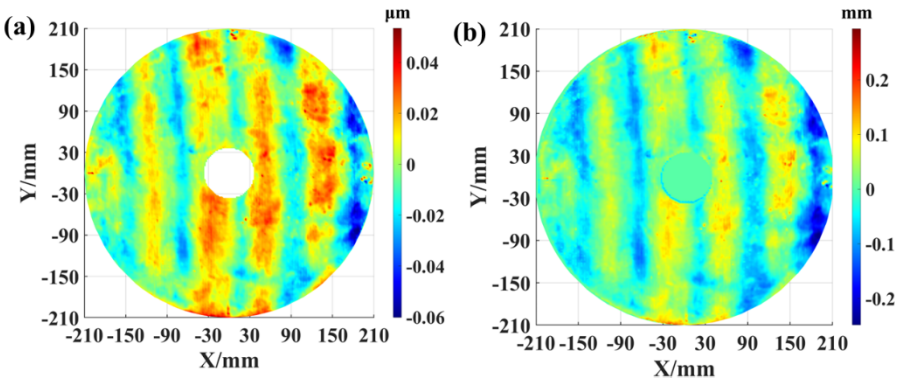

Fig. 16. (a) Periodic surface residuals caused by the changed polishing gap and (b) prediction of polishing gaps change with ARIMA.

Optics EXPRESS

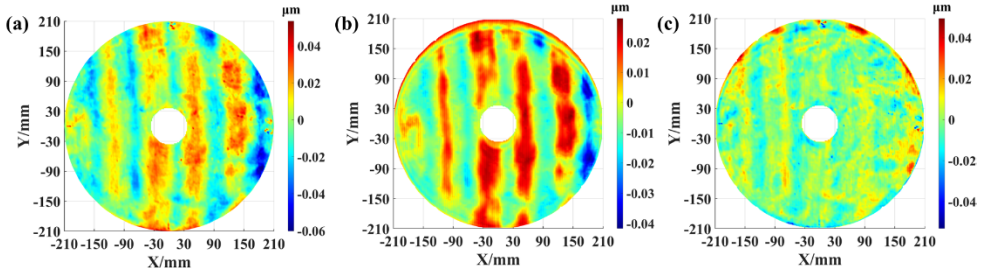

Fig. 17. Simulation verification of the prediction accuracy of polishing gap change. (a) Periodic surface residuals caused by the changed polishing gap; (b) simulation periodic surface residuals; and (c) prediction accuracy comparison.

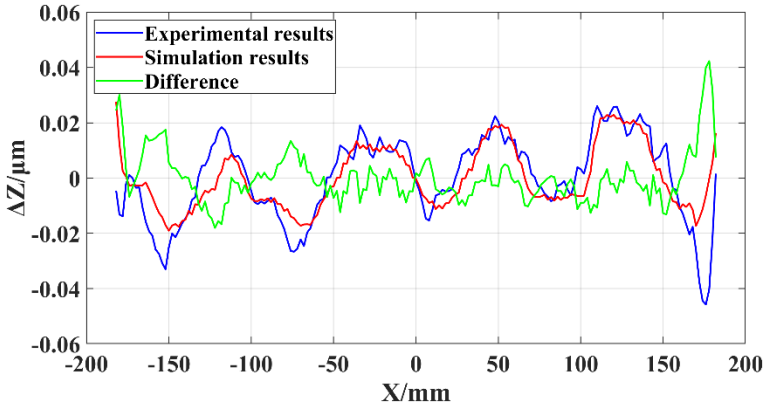

Fig. 18. Comparison curve of periodic surface shape errors between simulation and experiment along X-axis.

The formulation of the second polishing strategy and the polishing results. The input surface errors for the second polishing phase were periodic in nature, as depicted in Fig. 17(a). The TIF parameters for the second polishing were set identically to those for the first polishing. A convergence polishing strategy was implemented in the secondary polishing to address the periodic surface residuals. The dwell times were computed, and a polishing control program was generated with altered input TIFs. The results of the second polishing for the plane mirror are presented in Fig. 19. Notably, the second polished surface figures did not exhibit periodic errors, as evidenced in Fig. 19(b) and Fig. 20, aligning with the simulation results in Fig. 17(c). Additionally, the RMS after secondary polishing (RMS = 0.112λ) was virtually identical to that prior to polishing (RMS = 0.110λ), and the distribution of errors in both instances was nearly the same, as demonstrated in Fig. 21. These findings substantiate that the method proposed in this paper can accurately predict changes in TIFs and mitigate the effects of the robot-MRF's trajectory errors on polishing accuracy without altering the initial surface shape errors.

The formulation of final polishing strategy and polishing results. The input surface errors for the third polishing were depicted in Fig. 19(a), with RMS = 0.112 λ. The TIF parameters for the third and subsequent polishings were set identically to those for the initial polishing, and a convergence polishing strategy was again adopted. Dwell times were calculated, and a polishing control program was generated with variable TIFs. To discount the edge effect that might influence the polishing results, regions beyond ϕ80 mm and within ϕ399 mm were selected for the polishing outcomes. The surface accuracy was enhanced to 0.013 λ after three

Optics EXPRESS

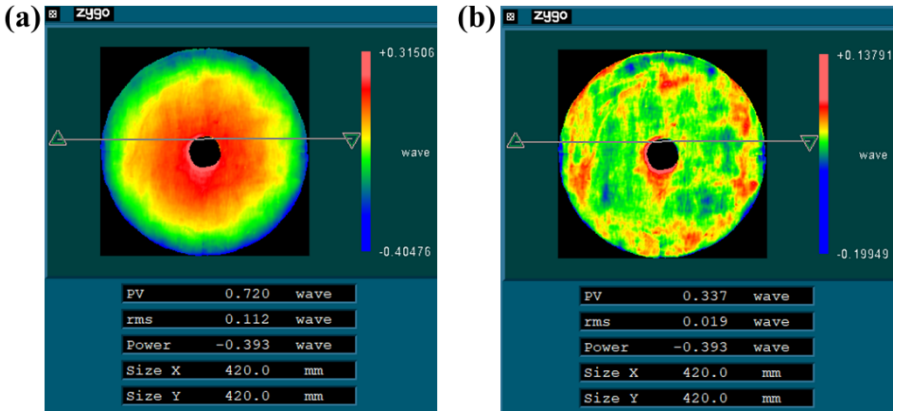

Fig. 19. Second polishing results of the plane mirror using the robot-MRF with prediction of TIFs change. (a) Surface figures without periodic errors: RMS = 0.112 λ; (b) Second polishing results showing that the primary aberrations (Power, Coma, Astigmatism, and Spherical aberration) are eliminated: RMS = 0.019 λ.

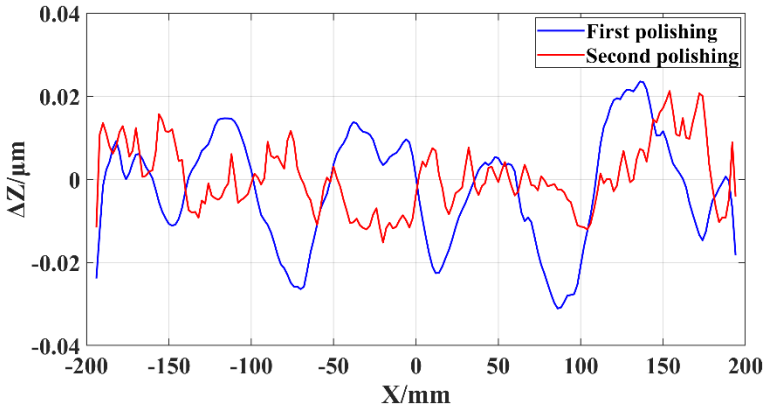

Fig. 20. Comparison curve of surface shape errors without the primary aberrations (Power, Coma, Astigmatism, and Spherical aberration) along X-axis after first and second polishing.

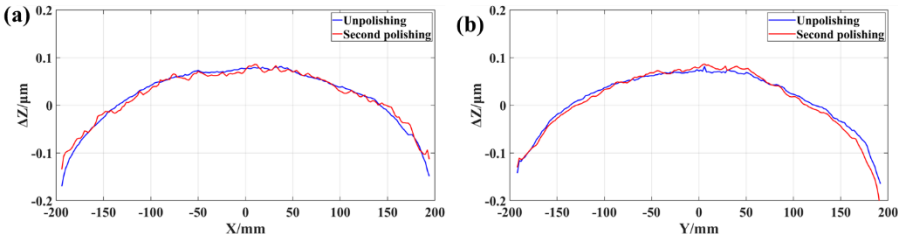

Fig. 21. Comparison curve of surface shape errors of unpolishing and second polishing. (a) Along X-axis; (b) Along Y-axis.

Optics EXPRESS

rounds of polishing, as illustrated in Fig. 22. The experimental data confirm that the robot-MRF possesses high-precision polishing capability without requiring trajectory error compensation. Moreover, no residual periodic errors stemming from the periodic variation of polishing gaps in the surface shape errors were observed, as shown in Fig. 23. Particularly, only MRF was used for polishing in this experiment. The final polishing accuracy reached 0.013 λ and failed to continue to improve due to the influence of middle-high frequency errors. However, this observation does not imply that the polishing accuracy limit of this method was reached. Additionally, although the method has not been verified on a curved mirror, the working orientation of the polishing wheel can remain parallel to the normal line of the curved surface owing to the six-dimensional motion control of the robot. The TIF of the MRF can be regarded as a unit plane compared to the entire surface, which is composed of many unit planes. The polishing of a curved surface can be regarded as the polishing of each unit plane; therefore, the method is also suitable for the high-precision polishing of curved optics.

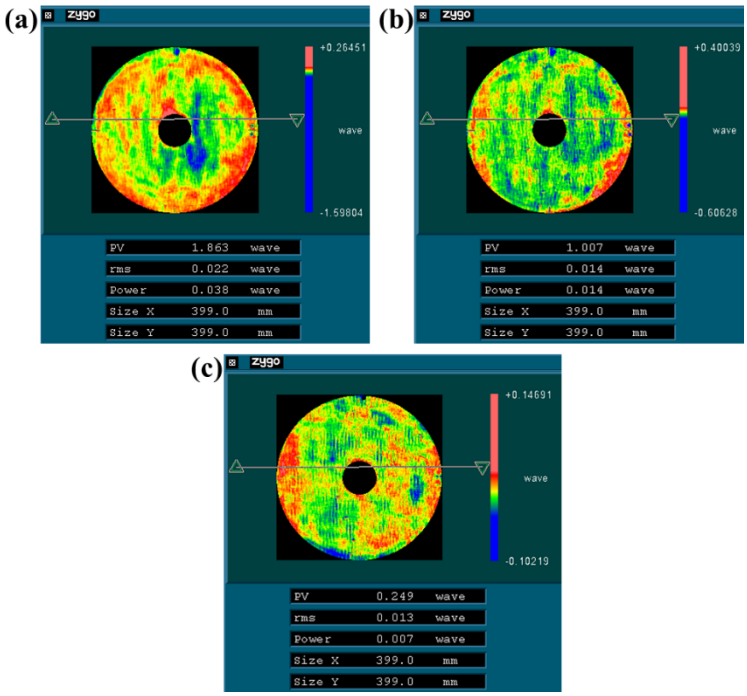

Fig. 22. Polishing results of the plane mirror using the robot-MRF with prediction of TIFs change (the area beyond ϕ80 mm and within ϕ399 mm). (a) Third polishing results: RMS = 0.022 λ; (b) Forth polishing results: RMS = 0.014 λ; (c) Fifth polishing results: RMS = 0.013 λ.

4.3. Verification of prediction accuracy of polishing gap changes

The trajectory errors of the equipment were examined using a laser tracker (FARO Vantage, 16 μm + 0.8 μm/m) and then compared with the predicted variations of the polishing gaps, with the aim of further verifying whether the systematic variations of TIFs that arise from the robot-MRF trajectory errors can be accurately predicted. The trajectory errors of the robot-MRF in the polishing state were examined, as shown in Fig. 24. The measuring coordinate system $\{O_{XYZ}\}$ of the laser tracker was set parallel to the workpiece coordinate system $\{O_{xyz}\}$, and the spatial sampling frequency of the laser tracker was set at 4 mm. Since the polished element was

Optics EXPRESS

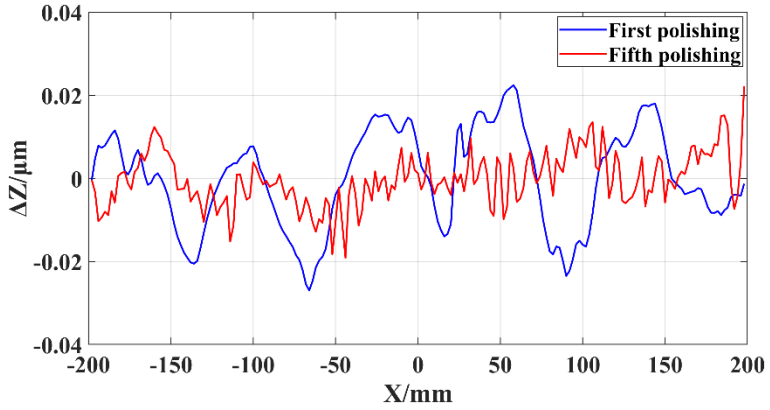

Fig. 23. Comparison curve of surface shape errors without the primary aberrations (Power, Coma, Astigmatism, and Spherical aberration) along X-axis after first and fifth polishing.

flat, the Z-value of the examination errors was considered the variations in the polishing gap attributed to the trajectory errors. Figure 25(c) presents the comparison between the examined Z-axis trajectory errors (Fig. 25(a)) and the predicted polishing gap variations (Fig. 25(b)). The prediction accuracy of the polishing gap variations was calculated as PV = 0.155 mm; the proportion of the prediction error PV < 0.1 mm reached 94.44%, and that of PV < 0.05 mm was obtained as 82.99%. Moreover, as indicated by the result, the whole comparison results generally followed a random distribution, suggesting that the variations of the systematic polishing gaps can be effectively predicted. The above-mentioned finding further confirmed that the method proposed in this study is capable of accurately predicting the variations of the polishing gap arising from systematic trajectory errors and further determining the distribution of TIFs' variation in the polishing process.

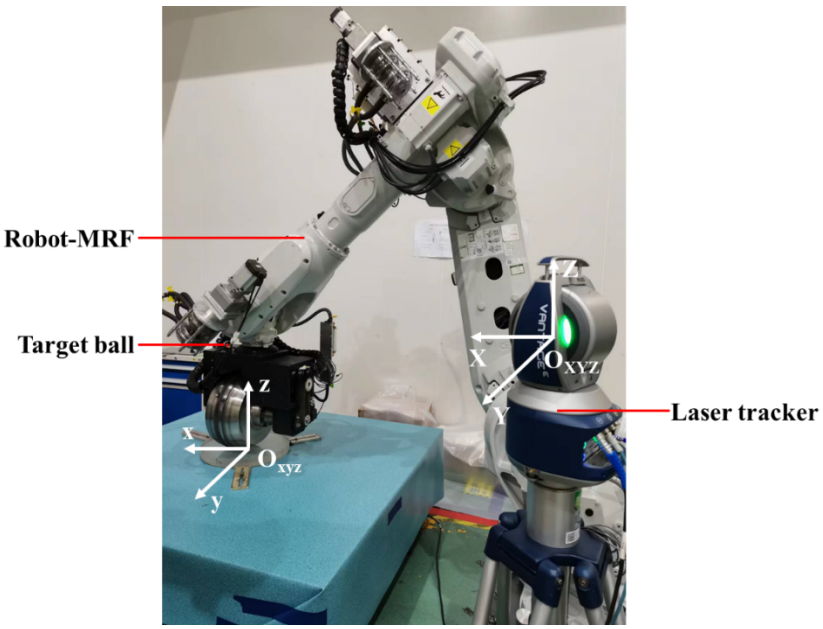

Fig. 24. Measurement of the robot-MRF trajectory errors.

Optics EXPRESS

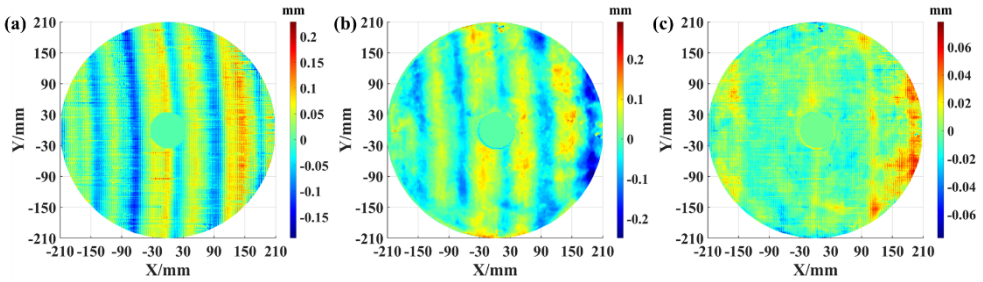

Fig. 25. Comparison of measurement and prediction errors. (a) The measured Z-axis trajectory errors, PV = 0.42 mm; (b) Predicted changes of polishing gap, PV = 0.54 mm; (c) Comparison of measurement and prediction errors, PV = 0.16 mm.

5. Conclusions

To solve the low trajectory error problems of robot-MRFs, affecting the polishing accuracy, this study developed a 3D MRF TIF model based on IDT by analysing the relationship between MRF MRR and polishing gap. A novel polishing method based on variable TIFs and surface figures of polished optics was used to determine the variations in the polishing gap. The variable TIFs were used to perform high-precision polishing to suppress the influence of the variations in the polishing gaps caused by the robot-MRF trajectory errors affecting the polishing precision. The polishing experiments showed that the robot-MRF could achieve high-precision polishing without compensations. The conclusions are summarised as follows.

(1) An MRF MRR model was established, demonstrating an exceptional level of agreement between theoretical and empirical findings. Moreover, both theoretical and experimental analyses revealed that the relationship between MRR and the MRF polishing gap was nonlinear.

(2) A 3D MRF TIF model, based on the IDT, was introduced to precisely predict the TIFs at differing polishing gaps. This model boasts an MRR prediction accuracy is less than 1%, which testifies to its ability to accurately anticipate the TIF under varied polishing gaps.

(3) A novel high-precision polishing method for the robot-MRF, based on variable TIFs and surface figures of polished optics, was introduced. This method, devoid of reliance on trajectory error-measuring apparatus or robot operating error compensation, demonstrated through simulation results its capacity to accurately predict changes in systemic polishing gaps during the process.

(4) High-precision polishing experiments were conducted on a ϕ420 mm fused silica plane mirror using the robot-MRF. The experimental results indicated that the polishing accuracy of the plane mirror can be improved from 0.11 λ RMS to 0.013 λ RMS by utilizing variable TIFs, and there were no systematic surface shape errors attributable to operational errors. The congruence between predicted and measured polishing gap results demonstrated that this method can accurately compute changes in the systemic polishing gap. Consequently, these findings verify that the method proposed herein can accurately predict changes in TIFs during polishing, and that it can utilise a low trajectory precision robot-MRF to achieve high precision polishing of the target, thus proving its applicability in the realm of high-precision optical polishing.

Funding. National Key Research and Development Program of China (2022YFB3403405); Youth Innovation Promotion Association of the Chinese Academy of Sciences (2021215); National Natural Science Foundation of China (62275246, 62075218, 12003034, 12203048).

Optics EXPRESS

Acknowledgments. The authors would like to thank the anonymous referees for their valuable suggestions and comments that have helped improve the paper.

Disclosures. The authors declare no conflicts of interest.

Data availability. Data underlying the results presented in this paper are not publicly available at this time but may be obtained from the authors upon reasonable request.

References

1. H. M. Martin, R. Allen, V. Gasho, B. T. Januzzi, D. W. Kim, J. S. Kingsley, K. Law, A. Loeffa, R. D. Lutz, T. J. McMahon, C. J. Oh, M. T. Tuell, S. N. Weinberger, and S. C. West, "Manufacture of primary mirror segments for the Giant Magellan Telescope," Proc. SPIE **10706**, 107060V (2018).
2. H. M. Martin, R. Ceragioli, V. Gasho, B. T. Jannuzi, D. W. Kim, J. S. Kingsley, K. Law, A. Loeff, R. D. Lutz, S. Meyen, C. J. Oh, M. T. Tuell, S. N. Weinberger, S. C. West, R. Whitsitt, and R. Wortley, "Production of 8.4 m primary mirror segments for GMT," Proc. SPIE **12188**, 121880J (2022).
3. J. Vernin, C. Muñoz-Tuñón, and M. Saranzin, *et al.*, "European extremely large telescope site characterization I: Overview," Publ. Astron. Soc. Pac. **123**(909), 1334–1346 (2011).
4. H. V. Ramió, J. Vernin, and C. Muñoz-Tuñón, *et al.*, "European extremely large telescope site characterization. II. High angular resolution parameters," Publ. Astron. Soc. Pac. **124**(918), 868–884 (2012).
5. K. Kamikawa, A. Nagaia, T. Ashidaa, K. Tania, T. Nariyamaa, T. Ishidab, J. Takakib, N. Kawaguchib, M. Endob, Y. Ezakib, T. Usudac, and M. Saitoc, "High precision machining in TMT (Thirty Meter Telescope) structure manufacturing," Proc. SPIE **114**, 1–9 (2020).
6. G. Derst and V. Giggel, "Fabrication technologies for large optical components at Carl Zeiss Jena GmbH," Proc. SPIE **7739**, 1–11 (2010).
7. D. Walker, C. Dunn, G. Yu, M. Bibby, X. Zheng, H. Wu, H. Li, and C. Lu, "The role of robotics in computer controlled polishing of large and small optics," Proc. SPIE **9575**, 1–9 (2015).
8. S. Wan, X. Zhang, M. Xu, W. Wang, and X. Jiang, "Region-adaptive path planning for precision optical polishing with industrial robots," Opt. Express **26**(18), 23782–23795 (2018).
9. L. Li, X. Li, Q. Cheng, R. Li, W. Deng, X. Luo, F. Zhang, D. Xue, and X. Zhang, "Optimized strategy to restrain the mid-spatial-frequency surface error in computer-controlled optical surfacing," Results Phys. **19**, 103356 (2020).
10. Z. Liu, B. Xie, and A. Wang, "The research of the precise aspheric wheeled polishing technology," Proc. SPIE **10827**, 1–7 (2018).
11. C. Wang, Y. He, Y. He, H. Zhang, C. Liu, L. Jiang, and L. Jiang, "Suppression of mid-spatial-frequency waviness by a universal random tree-shaped path in robotic bonnet polishing," Opt. Express **30**(16), 29216–29233 (2022).
12. L. Li, J. Zhang, C. Song, X. Zhang, X. Yin, and D. Xue, "New generation magnetorheological finishing polishing machines using robot arm," Proc. SPIE **11341**, 1134118 (2019).
13. K. Ren, X. Luo, L. Zheng, Y. Bai, L. Li, H. Hu, and X. Zhang, "Belt-MRF for large aperture mirrors," Opt. Express **22**(16), 19262–19276 (2014).
14. S. Wan, C. Wei, C. Hu, G. Situ, Y. Shao, and J. Shao, "Novel magic angle-step state and mechanism for restraining the path ripple of magnetorheological finishing," Int. J. Mach. Tool Manu. **161**, 103673 (2021).
15. L. Zhang, C. Zhang, and W. Fan, "Robotic magnetorheological finishing technology based on constant polishing force control," Appl. Sci. **12**(8), 3737 (2022).
16. R. Cheng, L. Li, X. Li, Y. Bai, X. Luo, D. Xue, and X. Zhang, "High-precision magnetorheological finishing based on robot by measuring and compensating trajectory error," Opt. Express **30**(25), 44741 (2022).
17. B. Zhong and Q. Xu, sJ. Wang, W. Deng, and X. Chen, "Evaluation and compensation of a kinematic error to enhance prepolishing accuracy for large aspheric surfaces by robotic bonnet technology," Opt. Express **28**(17), 25085–25100 (2020).
18. Y. Bai, X. Zhang, C. Yang, L. Li, and X. Luo, "Material removal model of magnetorheological finishing based on dense granular flow theory," LAM **3**(4), 630–631 (2022).
19. S. Liu, H. Wang, Q. Zhang, J. Hou, B. Zhong, and X. Chen, "Regionalized modeling approach of tool influence function in magnetorheological finishing process for aspherical optics," Optik **206**, 164368 (2020).
20. O. Babak and C. V. Deutsch, "Statistical approach to inverse distance interpolation," SERRA **23**(5), 543–553 (2009).
21. H. Yang, Q. Zhang, Z. Zhu, W. Fan, Y. Zhang, and W. Huang, "Dynamic approximation method for removal function size in magnetorheological finishing," Opt. Eng. **58**(9), 095103 (2019).
22. L. Li, D. Xue, W. Deng, X. Wang, Y. Bai, F. Zhang, and X. Zhang, "Positive dwell time algorithm with minimum equal extra material removal in deterministic optical surfacing technology," Appl. Opt. **56**(32), 9098–9104 (2017).
23. P. Ramos, N. Santos, and R. Rebelo, "Performance of state space and ARIMA models for consumer retail sales forecasting," Robot CIM-INT Manuf. **34**, 151–163 (2015).
24. D. A. Tedjopurnomo, Z. Bao, B. Zheng, F. M. Choudhury, and A. K. Qin, "A survey on modern deep neural network for traffic prediction: Trends, methods and challenges," IEEE Trans. Knowl. Data Eng. **34**(4), 1544–1561 (2020).
25. I. Amidror, "Scattered data interpolation methods for electronic imaging systems: a survey," J. Electron. Imaging. **11**(2), 157–176 (2002).